6-1-2020

Beta-delayed charged-particle spectroscopy using TexAT

J. Bishop
Cyclotron Institute

G. V. Rogachev
Cyclotron Institute

S. Ahn
Cyclotron Institute

E. Aboud
Cyclotron Institute

M. Barbui
Cyclotron Institute

See next page for additional authors

Recommended Citation

Bishop, J., Rogachev, G., Ahn, S., Aboud, E., Barbui, M., Baron, P., Bosh, A., Delagnes, E., Hooker, J., Hunt, C., Jayatissa, H., Koshchiy, E., Malecek, R., Marley, S., O'Dwyer, R., Pollacco, E., Pruitt, C., Roeder, B., Saastamoinen, A., Sobotka, L., & Upadhyayula, S. (2020). Beta-delayed charged-particle spectroscopy using TexAT. *Nuclear Instruments and Methods in Physics Research, Section A: Accelerators, Spectrometers, Detectors and Associated Equipment, 964* https://doi.org/10.1016/j.nima.2020.163773

Version of Record: https://www.sciencedirect.com/science/article/pii/S0168900220303089
Manuscript_ec4c9b4fb98f5f5d56590c285171d623

Beta-delayed charged-particle spectroscopy using TexAT

J. Bishop[a,b], G.V. Rogachev[a,b,c], S. Ahn[a,b], E. Aboud[a,b], M. Barbui[a], P. Baron[d], A. Bosh[a,b], E. Delagnes[d], J. Hooker[1,a,b], C. Hunt[a,b], H. Jayatissa[2,a,b], E. Koshchiy[a], R. Malecek[e], S.T. Marley[e], R. O'Dwyer[a,b], E.C. Pollacco[d], C. Pruitt[f], B.T. Roeder[a], A. Saastamoinen[a], L.G. Sobotka[f], S. Upadhyayula[a,b]

[a] *Cyclotron Institute, Texas A&M University, College Station, TX 77843, USA*
[b] *Department of Physics & Astronomy, Texas A&M University, College Station, TX 77843, USA*
[c] *Nuclear Solutions Institute, Texas A&M University, College Station, TX 77843, USA*
[d] *IRFU, CEA Université Paris-Saclay, F-91191, Gif-sur-Yvette, France*
[e] *Department of Physics and Astronomy, Louisiana State University, Baton Rouge, LA 70803*
[f] *Department of Chemistry, Washington University, St. Louis, MO 63130, USA*

Abstract

β-delayed charged-particle emission is a sensitive probe of three-body decays in light nuclei. Time Projection Chambers (TPCs) offer a significant advantage over traditional charged-particle spectroscopy techniques due to a low-energy threshold and a high-geometric efficiency ($\approx 4\pi$) which are essential for use with radioactive ion beams where the beam intensities are limited. The technique for high-sensitivity spectroscopy of β-delayed charged-particle emission is shown to be possible using the Texas Active Target (TexAT) TPC in conjunction with the General Electronics for TPCs (GET) system. The benchmark case studied was that of ^{12}N β-decay to the first α-unbound state in ^{12}C, the Hoyle state. Half-life and branching ratio measurements are presented and are in good agreement with previous studies. The efficacy of using TPCs to study such a near-threshold state and disentangle the three-body dynamics of the decay products is demonstrated.

Keywords: TPC, Charged-particles, Active target, Nuclear, Beta-decay

Email address: jackbishop@email.tamu.edu (J. Bishop)
[1]Present address: Department of Physics and Astronomy, University of Tennessee, Knoxville, Tennessee 37996, USA.
[2]Present address: Physics Division, Argonne National Laboratory, Argonne, Illinois 60439, USA.

1. Beta-delayed particle decay

β-delayed particle decay can occur where the daughter nucleus has states, populated by $\beta^{\pm}$ decay, which are above the particle decay threshold. This emission can be used for the study of a selective population of states as allowed by the β-transition rules. For instance, in ^{12}C, one can use the decay of ^{12}N/^{12}B to populate states above the α-decay threshold. Isospin symmetry can also be measured here by examining the relative branching ratios of states. Additionally, the strength of the population can be used as a probe of the 3-α cluster structure which will give a reduced B_{GT} [1, 2]. A typical β-delayed charged-particle measurement is performed by implanting beams in a thin foil and measurement of the products with a surrounding shell of silicon detectors. For states with a small break-up energy, however, there are significant difficulties with particles having sufficient energy to escape the foil, pass through the silicon dead layer, and be measured above the detection threshold (e.g. [3]) as well as the energy deposition of the correspond β-particle. Instead of using a thin target and silicon detectors, one can use an active target TPC which is simultaneously the stopping and detector medium so the full decay energy is recovered. The low density of the detector medium also practically eliminates issues associated with β-particle related background and reduces the energy smearing due to the electron/positron energy loss in the detector medium.

This TPC method has been previously used to study near proton threshold resonances by measuring the total decay energy in the daughter nucleus (e.g. [4]) using a calorimetric technique. In the region of light nuclei, multiple-particle decays are possible for nuclei far from stability. The energy partition between these multiple particles from the decay is important to understand the structure of the decaying state. While the energy partition cannot be measured in calorimetric setups, tracks of separate particles in the detector system described here can be measured and their energy can be recovered either by a total energy integration or via the particle's range. A test case of $^{12}\mathrm{N} \rightarrow {}^{12}\mathrm{C}^{\star}$ was chosen as its β-decay branching ratios have been well measured [3]. Additionally, the "Hoyle state" at 380 keV above the 3-α threshold [5] has been subjected to very accurate measurements of

its branching ratio between sequential α-decay through the ^{8}Be(g.s) or directly into 3-α [6, 7, 8, 9]. A high sensitivity (BR $< 10^{-4}$) measurement of this 3-α branching ratio is very difficult in both the calorimetric TPCs and the thin foil experiments and previous measurements can serve as a benchmark of the branching ratio sensitivity for further β-delayed three-body decays.

2. TexAT detector

The β-delayed charged-particle emission was studied using the Texas Active Target detector system. It is a state-of-the-art active target time projection chamber that was designed to study structure of exotic nuclei, clustering phenomena, nucleon transfer and fusion reactions with rare isotope beams. The detailed technical description of TexAT is given in Ref. [10]. The detector was commissioned in August of 2017 and the results of the commissioning run, in which the structure of the exotic nucleus ^{9}C was studied, are published in Ref. [11]. It is a versatile detector which can be used for a wide variety of experiments. The active region of the TPC is 224 x 245 x 135 mm^3, over which a uniform electric field is placed, large enough to measure tracks of charged particles. Electrons generated by charged particles ionizing the detector gas, are drifted towards a Micromegas (MICRO MEsh GASeous) plate detector. This plate has a high electric field applied across a 128 μm gap to make electron multiplication using avalanche amplification before approaching the Raether limit [12]. The amplified electron-induced signal is read out by segmented pads providing the position sensitivity. This plate lies in the xy-plane with the beam entering the chamber along the y-axis. The central region (6 x 128 pads) is segmented in such a way that each individual 1.75 x 3.5 mm pad is read out. Outside of the central 6 pads, multiplexing along the y-direction into so-called 'chains' and along the x-direction into so-called 'strips' reduced the amount of readout channels required.

The original TexAT configuration, detailed in [10], does not have any additional electron multipliers other than a Micromegas detector. As made clear from the discussion in Sec. 3, low gas pressure is required for spectroscopy of near-threshold states. To provide additional

gain at low gas pressures, THick Gas Electron Multipliers (THGEM) [13] were placed directly above the Micromegas. The next section describes this upgrade of the TexAT detector.

3. Experimental details

The experiment was performed using the K500 cyclotron at the Cyclotron Institute at Texas A&M University. A ^{12}N beam (typical intensity of 60 pps) was created via the interaction of a 11 AMeV ^{10}B primary beam undergoing a ^{3}He(^{10}B, ^{12}N)n reaction in a gas cell placed upstream of the MARS (Momentum Achromatic Recoil Spectrometer) [14]. MARS can then select and deliver the ^{12}N secondary beam to the TexAT chamber. The beam contaminant was ^{7}Be which was fully separated in the offline analysis. This secondary beam was extracted at 6 AMeV but was slowed to $\sim$ 2 AMeV as it entered the chamber by the use of an aluminum degrader (61.6 μm at 14°) attached to a turntable allowing fine energy tuning such that the beam stopped in the center of the TexAT detector. To allow for this final energy loss, and also to provide the detector medium, TexAT was filled with 20 Torr CO_2 (TexAT is not operating in 'active target' mode here and this gas serves as the detection medium only). This constituted the smallest pressure that could stop all the α-particles of interest inside the Micromegas region. Offline measurement of this gas pressure showed fluctations of $< \pm 2$ Torr during the experimental campaign and was calculated and corrected for each 1 hour of beam time. The voltage across the Micromegas, THGEM and field cage were 445 V, 500 V and 500 V respectively. An overview of the experimental setup is shown in Fig. 1.

3.1. THick Gas Electron Multipliers (THGEM)

The THGEM, similarly to the Micromegas, provides a large signal gain via a high electric field across a small region inducing electron multiplication. Enough signal gain can be achieved by this two-fold amplification with a relatively low electric field. The electric field across the 1.25 mm thick THGEM was 0.4 $\times 10^4$ V/cm in comparison with the much larger 3.5 $\times 10^4$ V/cm on the Micromegas. In the previous test without the THGEM, the Micromegas bias was required to be 3.9 $\times 10^4$ V/cm to achieve a slightly smaller amplitude

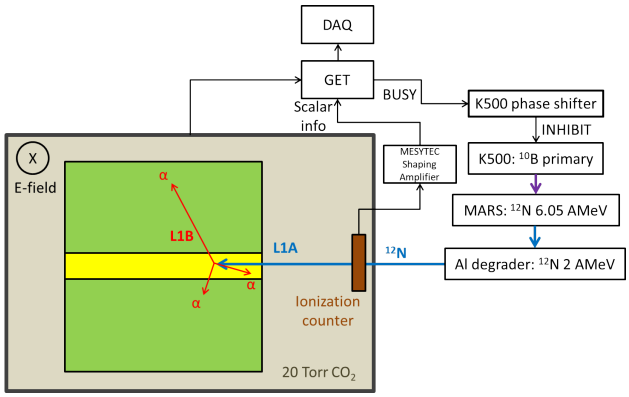

Figure 1: Schematic of the experimental setup showing the link between the GET MuTanT (MUltiplicity Trigger ANd Time) module and the Cyclotron phase shifter. The beam is inhibited whenever the MuTanT provides a busy signal. This corresponds to when an L1A trigger is received and MuTanT is waiting for up to 30 ms for a L1B trigger. Upon this second trigger, the busy signal is turned off following the reading of the waveforms.

signal than with the upgraded combined system. The reduction in the Micromegas field reduces sparking issues prevalent at low pressures near the minimum of the Paschen curve [15].

3.2. Single event counting

To detect the incoming beam, an ionization counter (IC) was used which allowed for particle-by-particle counting. This IC signal was fed into a scalar for later use as well as being passed into the GET (General Electronics for TPCs) system [16] and the waveform was digitized with a sampling rate of 10 MHz for 512 time-buckets (equivalent to 51.2 μs in total length per signal).

In an effort to ensure that only one ^{12}N per event was present in TexAT, the GET provided a busy signal which was fed to the K500 cyclotron phase shifter to prevent further ^{10}B, and therefore ^{12}N, from being accelerated/produced. This beam veto lasted for 30 ms or until the busy signal is cleared (discussed below). This signal takes approximately 0.1 ms to shift the cyclotron phase, therefore it is possible to have two beam particles in TexAT. These events were removed in the offline analysis.

This setup therefore implants a single ^{12}N that subsequently decays inside the Mi-

cromegas region. The dominant ^{12}N decay branches are to the ground-state (96.2%) and the first gamma-decaying excited-state of ^{12}C (1.9%) at 4.44 MeV. The ^{12}C-recoil energy of $<$ 10 keV is below the threshold of the Micromegas and the recoil range does not extend over more than one pad. One pad triggers were excluded by the pad multiplicity, m, trigger track requirement (m$\geq$2). Only the $\sim$ 2 % branching ratio to states above the 7.27 MeV triple-α threshold which decay into three α-particles can be detected. A full event is therefore characterized by the implantation and the subsequent decay into 3 α-particles.

3.3. 2p mode

The trigger mode for this experiment is specifically implemented by GET to require two separate triggers in time before the data are digitized and recorded. This trigger mode is called the "2p mode" as it was originally designed to measure 2-proton decay. In this mode, the 512 switched capacitor array (SCA) cells are split into two of 256 cells, providing 256 time-buckets for each half-event. A full event includes two correlated half-events. The separate triggers for each half-event may have different channel and time multiplicity conditions with the first and second triggers known as L1A and L1B, respectively. In our case, the L1A trigger corresponds to the implantation of the ^{12}N into the TPC while the L1B relates to the decay of $^{12}C^{\star} \rightarrow 3\alpha$. The trigger for L1B was carefully selected such that low-energy events (the first α-unbound state) are not excluded but the trigger level is above the noise by employing a m$\geq$ 2 trigger. The time between the L1A and L1B trigger is also stored and is referred to as the D2P time. For the correct settings of the L1A and L1B trigger modes, the D2P time should follow the decay curve for the ^{12}N with a half-life of 11.000(16) ms [17]. If an L1B trigger is successfully received, the busy signal, sent to the K500 phase shifter, is removed (after the read/write of the waveforms by the DAQ), the cyclotron is returned to normal operation and the primary beam is sent back onto the production target. If no L1B trigger is received after a L1A trigger, there is a time-out of 30 ms. For this experiment, these half events (corresponding to beam implantation and decay to the ground or first excited state) were also stored for completeness. This option was chosen so that if the β-decay occurs outside of the 30 ms time window, the event will be recorded as two separate

L1A events (beam implantation and then decay). The stopping point of the beam (from the first L1A half event) and the decay center (from the second L1A half event) should then match if these correspond to the same implantation + decay so these otherwise lost events can be recovered. Additionally, recording these events also helped for beam normalization purposes as each half L1A event can be verified as resulting from ^{12}N via the energy loss in the gas. The beam energy resolution after the upstream degrader was sufficiently large (5 %) that the beam range was spread out over the Micromegas detector. This allows improved rejection of uncorrelated events, see Sec. 6.2. The electronics store the global time of each event and therefore one can also reconstruct the D2P time and use it to measure the decay times much greater than the 30 ms beam veto.

4. Data analysis

4.1. Event merging

The employed L1A/L1B (implant/decay) trigger logic will throw away events where the decay time exceeds 30 ms. Therefore, unpaired L1A events were merged to increase the statistics of the overall 3-α events as well as to constitute an initial pruning of events. At this stage, the IC waveform was fitted and the events corresponding to the lower amplitude ^{7}Be contaminant were removed. For the full L1A/L1B events, there was an issue with the MFM [18] (Multi-Frame MetaFormat) file where the L1A and L1B sub-events were being incorrectly labeled. Accordingly, one could not be sure without additional checks to establish which half-event corresponded to the first trigger and which gave the second trigger. The L1A sub-event was then labeled as that being in coincidence with the IC signal therefore being the sub-event from a validated beam implantation. Later analysis confirmed the beam/decay identification using a Hough transform [19]. The waveforms were also subjected to a baseline subtraction procedure. The GET electronics have Fixed Pattern Noise (FPN) channels which are read out and used to measure the baseline offset of the waveform over time. These FPN channels, however, were not indicative of the baseline shifts seen in the waveforms connected to the Micromegas. Instead, a simple offset baseline

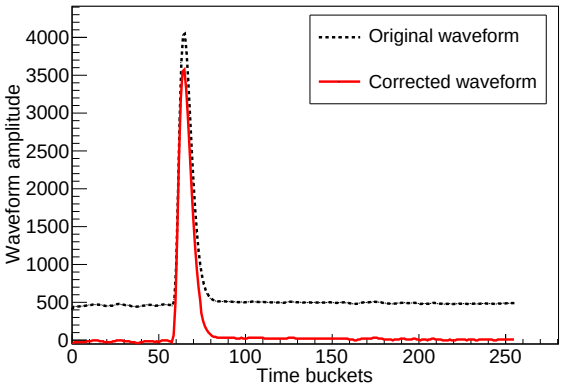

Figure 2: Waveform for a single Micromegas channel demonstrating the modification of the original waveform (black) to the corrected waveform (red) via the subtraction of a baseline which is evaluated for each channel using the modal value across the 256 timebuckets.

subtraction was performed where the baseline value was chosen by the modal value across the 256 time buckets of the waveform for each Micromegas channel. Figure 2 shows typical waveforms before and after baseline correction.

4.2. Waveforms

The waveforms from the segmented Micromegas pads are fully digitized via the GET system after shaping and amplification. Each waveform takes (2 x 256) 12-bit samples every 100 ns. Analysis of these waveforms allows for the particle tracks to be fully reconstructed.

With the selected GET shaping time (0.5 μs), the signals arising from two different α-particle tracks can overlap as seen in the waveform shown in Fig. 3. To disentangle these different tracks, a deconvolution technique (1D Gold algorithm [20]) is used where the response function is taken from the internally generated pulser in the GET electronics. From this deconvoluted waveform, the timing and energy information can be extracted for multiple hits. A fit of the de-convoluted spectrum is then used to get the centroids of the peaks (which give the times), accurate energies from the integrals, and measures of the widths of the peaks. This deconvolution technique is seen to work well enough to separate two distinct peaks when the centroids are separated by more than 5 time buckets. This corresponds to a 0.5 μs time separation or around 6 mm in the vertical direction.

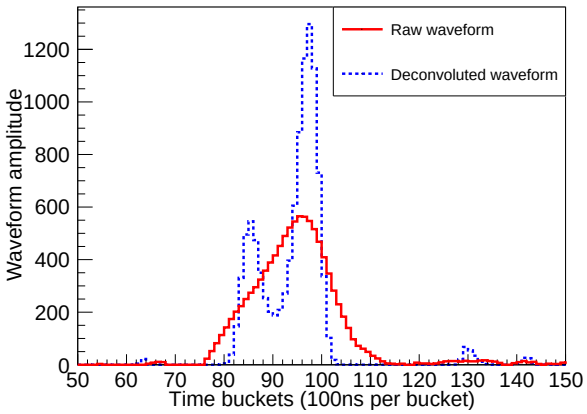

Figure 3: An example waveform for a single Micromegas channel. The raw waveform (red) can clearly be seen to have two components corresponding to two tracks separated in the vertical (time) direction. By deconvoluting this waveform using the GET response function, the deconvoluted waveform (blue) is obtained. The two peaks can then clearly be resolved. The peak of each of these fits and the integral is then used for the time and energy respectively.

Due to the large energy deposition at the decay vertex and the higher energy deposition of the implanted ^{12}N, there are channels which have saturated waveforms. To retain accurate energy information, this waveform is fit with the known waveform function to recover the energy and also an accurate time. This technique is currently incongruent with the deconvolution technique therefore any tracks which are saturated and overlapping cannot be separated. This does not strongly affect the track reconstruction as saturated signals only occur at or around the decay vertex where the three tracks have a very small separation, too close for the deconvolution technique to differentiate distinct tracks.

4.3. Track reconstruction

Given a set of hits with a given energy and time signal, the track of the particles can be reconstructed. For the central pad region, this is simple. However, for the side strips and chains region, this requires more input. As a particle traverses this region, it triggers a large number of both strips and chains. Due to the multiplexing (see [10] for more information), it is not immediately possible to match the progression in the x-direction (dictated by the chains) with that in the y-direction (dictated by the strips). To match an x and y hit, timing

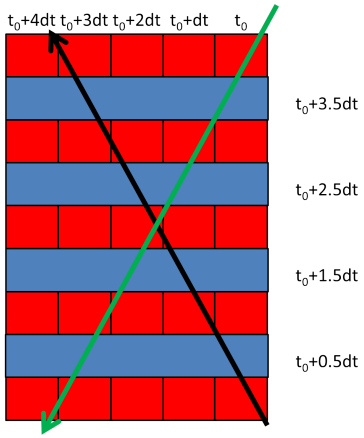

Figure 4: Strip/chain reconstruction. By comparing the time between the strips (blue) and chains (red), the correct track orientation shown in black can be differentiated from the incorrect track shown in green which has the same hit pattern.

is used. As a particle crosses between strips and chains (provided it is not extremely well localized in the x-y plane) the time for the subsequent hits should be increasing or decreasing depending on whether the particle is traveling up or down respectively. Therefore, to match strips and chains, the nearest pairings in time provide this reconstruction (shown in Fig. 4). If the particle travels parallel to the Micromegas plate, no such time-matching is possible and other techniques must be used. While these techniques work well for single particle tracks, they cannot be applied for multiple particle tracks. Therefore, events where the decay plane coincides almost exactly with the Micromegas plane must be identified and treated separately.

Following this reconstruction prescription, the L1A and L1B events were analyzed to give information about the decay process. Firstly, the L1A trigger was used to verify (by the energy deposition along the Micromegas and the amplitude of the IC signal) that the implantation corresponded to ^{12}N. This provides a near perfect differentiation of the ^{12}N from the ^{7}Be beam contaminant. The stopping point of the ^{12}N implants were then extracted.

An additional check was made to ensure that the measured L1A beam implantation corresponds to the L1B decay. The L1A stopping point of the beam is measured by taking the end-point of the track and is compared to the center of the 3-α decay. The distribution

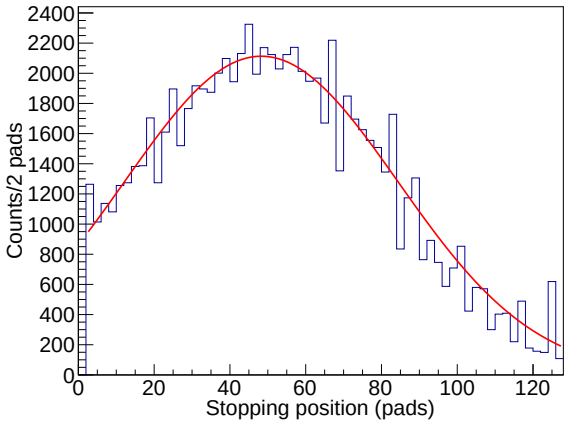

Figure 5: Stopping point distribution along the beam direction for the ^{12}N beam from a single 1-hour run fitted with a Gaussian (red). The distribution is determined by the initial energy spread of the secondary beam from the recoil separator as well as straggling effects in the aluminum degrader and entrance window. This large stopping point spread can be exploited to ensure that the beam implant and decays are correlated. 1 pad here corresponds to 1.75 mm.

of beam stopping points along the beam axis is shown in Fig. 5. Given the half-life of around 11 ms, the ^{12}N can undergo a random walk in the gas before the decay. Given a mean free path of 5 μm and a thermal velocity of 800 m/s, the expected average displacement σ is approximately 7 mm in 3D. The stopped beam ion is also assumed to be neutralized such that there is no residual ion drift due to the electric field. The center of the decay in the L1B should therefore be separated by a small number of pads. In the L1B trigger, one has no absolute time reference frame so the height of the decay in the detector is unknown. Therefore, the separation from the L1A implant is only in 2D (xy plane) with an expected Gaussian with $\sigma = 7$ mm. There are also errors from misidentification of the decay center which creates a displacement distribution as seen in Fig. 6 where the geometrical factor $r\ dr$ must be incorporated into the fit, hence at r=0 there are no counts. The extracted 9.3 mm shows that the Gaussian random walk dominates with the other factors adding only modest additional dispersion.

An example reconstructed track is shown in Fig. 7 where the L1A (yellow) and L1B (blue) tracks are overlaid showing how the decay vertex overlaps well with the stopping

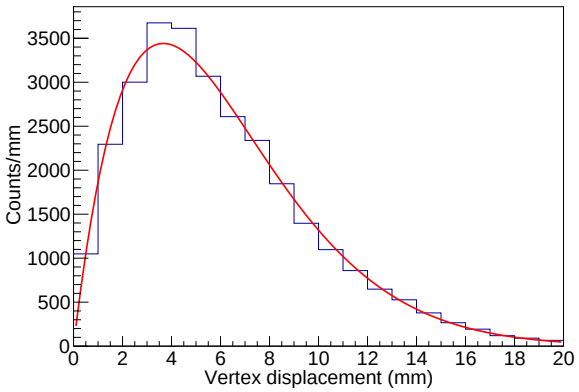

Figure 6: XY distance from the L1A beam implant stopping point to the fitted decay vertex for the L1B decay. The solid red line is the fit of the form $f(r) = r\exp(-(r-r_0)/2\sigma^2))$ where the additional factor of r allows for the greater area in dr at distance r. $\sigma = 9.3(5)$ mm is in reasonable agreement with the predicted $\sigma = 7$ mm solely from the random walk showing this is the dominant contribution.

point of the beam.

4.4. Excitation function

As with calorimetric TPCs, the total energy of the decay products can be measured and used to identify the populated states in ^{12}C. The excitation function from our TPC is shown in Fig. 8. The peak corresponding to the Hoyle state is clearly visible and is separated from the broader continuum at higher energies. The broad bump corresponds to a mixture of higher excitation energy states where the α-particles have sufficient energy to escape and therefore do not deposit their full energy in the TPC. This was verified by ensuring that the events in this peak have a track which borders the edge region of the TPC. Events below 8 MeV were then selected for further analysis. It is worth noting that one also removes any contribution from the Hoyle ghost peak [21] with this selection. The ghost peak arises where the penetrability factor for a near-threshold state rises faster than the decaying tail of the Breit-Wigner and therefore a secondary 'ghost' peak can appear from a single resonance.

4.5. Hoyle identification

As the Hoyle state decays predominately sequentially via ^{8}Be, one α-particle has a fixed energy of 190 keV while the remaining two α-particles can share the remaining 190 keV with

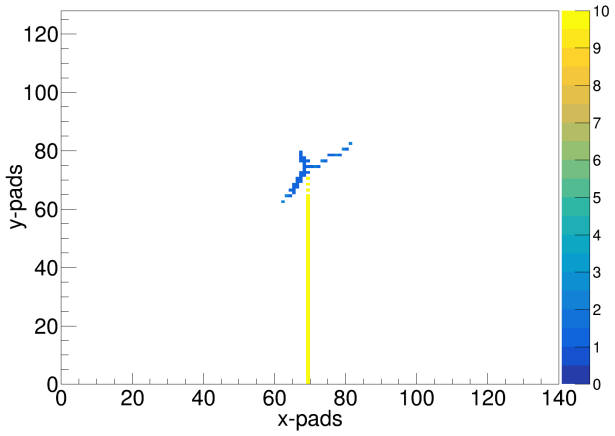

Figure 7: A real event from the experiment showing the xy projection of the L1A (yellow) and L1B (blue) events. The three arms from the decay of $^{12}C^{\star}$ can clearly be seen. The decay vertex can also be seen to clearly overlap with the stopping position of the implanted ^{12}N.

any energy split possible defined by the ^{8}Be decay angle, relative to the original $^{12}C^{\star}$ decay direction. This can be expressed as:

$$E_1 = \tfrac{2}{3}Q_1 \tag{1}$$

$$E_2 = \tfrac{Q_1}{6} + \tfrac{Q_2}{2} + \sqrt{\tfrac{Q_1 Q_2}{3}}\cos(\theta_{\mathrm{Be}}) \tag{2}$$

$$E_3 = \tfrac{Q_1}{6} + \tfrac{Q_2}{2} - \sqrt{\tfrac{Q_1 Q_2}{3}}\cos(\theta_{\mathrm{Be}}), \tag{3}$$

$$\tag{4}$$

with Q_1 denoting the $^{12}C(0_2^+) \rightarrow {}^{8}$Be(g.s)+$\alpha$ Q-value (287 keV), Q_2 denoting the Q-value for ^{8}Be(g.s) $\rightarrow 2\alpha$ (92 keV) and θ_{Be} the ^{8}Be decay axis relative to its momentum vector. Because the α-particles have energies well below the Bragg peak, the largest energy deposition from the L1B event occurs at the decay vertex. To find this decay center, the highest energy voxel is found with an additional weighting from the L1A known beam implantation position describing the probabilistic random walk. To ensure the highest energy density region is selected, the surrounding 26 voxels are also examined.

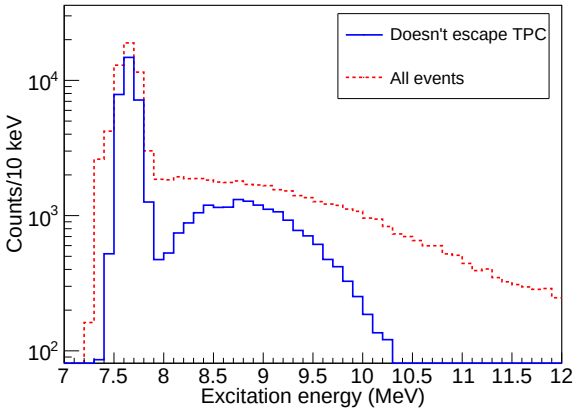

Figure 8: Calculated excitation function for measured states in ^{12}C. The continuum above the peak at 7.65 MeV is from higher lying states that do not deposit their full energy in the TPC as well as broad 0^+ states above the Hoyle state. The blue spectrum shows a selection to remove events where any of the tracks escape, hence removing the contribution from the higher lying states. Above 10.2 MeV, one of the break-up α-particles from the decay must have sufficient energy to escape the TPC. This agrees well with the termination point of the spectrum.

4.5.1. Length of longest arm

Another event selection tool is to find the voxel with the largest distance from the decay center which, for sequential decay, should correspond to the end-point of the track for a 190 keV α-particle. The corresponding distance is 38 mm. A value smaller than this with the same excitation energy is an indication of direct decay. However, Geant4 simulations indicated that such low energy α-particles can undergo significant scattering reducing the point-to-point distance. This additional lateral and longitudinal straggling effect can be as large as $\sim$10%.

Given the beam energy spread, it is possible the stopping point of the beam is not sufficiently well located in the center of the Micromegas therefore it is possible that one of the α-particles from the decay escaping the active region. The ^{12}N decay also provides a reasonable branching ratio to higher lying states, such as the 12.7 MeV state, and these α-particles easily escape and as such they contribute to the broad continuum seen above the Hoyle state peak. If any track is detected near the outer 10 mm of the Micromegas,

this event is discarded. After selecting the events of the correct energy, the length between the center of the decay and the furthest-point from this position is shown in Fig. 9. A well-isolated peak can indeed be seen and corresponds to roughly the length expected for the 190 keV α-particle. The large width of the peak is largely explained by straggling, finite pixellation effects and misidentification of the exact decay center.

To allow for a full determination of the energy sharing of the three α-particles, a Hough transform was used to find the three α-particle tracks. The Hough transform technique is well developed for TPC applications and has been demonstrated to work well in noisy environments. The difficulty here, is attaining reliable results with short tracks, a relatively large granularity and deviations from straight tracks.

4.5.2. Other decay arms

As well as the longest decay arm, the additional two arms of the decay (from the decay of the ^{8}Be(g.s) in the sequential case) also encapsulate important information about the decay. The momentum vectors of the shorter two arms were therefore extracted in a similar way to that of the longest arm. All voxel hits corresponding to the longest arm (by selecting voxels within 5 mm of the line from the decay center to the end of the arm) were removed and the next furthest point was found. This procedure was then repeated again to find the shortest arm. Due to the kinematics of the sequential decay, a colinear decay is possible where one of the α-particles is left at rest. An additional check was made to select this subset of events where a third arm was so short that the event can be described as colinear. Such decays cannot be direct.

For the events where three arms are successfully found, the decay energy, E_{decay}, can be calculated by converting the range into energies and then summing these energies. The excitation energy is then simply $E_x = E_{\mathrm{decay}} - Q$ (Q= - 7.27 MeV here). This value is a good indication of the correct reconstruction of the event track and the subsequent correct identification of the decay arms as well as providing a check of how the gas pressure changes throughout the experiment. Finally, a least-χ^2 fit was performed to minimize the distance between the voxels and the nearest of the three arms. Figure 10 shows the result of the two

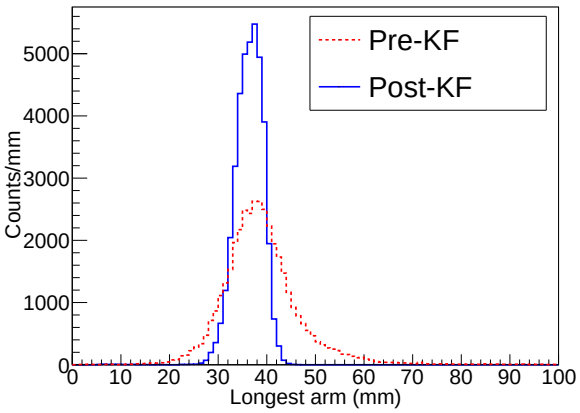

Figure 9: Distance between the measured decay center and the furthest part of the decay tracks after gating on the Hoyle state energy. The peak around $\sim$ 38 mm corresponds to the 190 keV α-particle from the decay of the Hoyle state. This value is shown for both before and after the kinematic fitting (KF) process.

different techniques for determining E_x compared to one another. The resolution (FWHM) from taking the full track is better than that of the calorimetric method (100 keV vs 175 keV).

4.6. Kinematic fitting

To improve the resolution of the tracks, the kinematic fitting (KF) technique was used. While this is more often used in particle physics [22], it has the exact same applications in nuclear physics decay experiments (see [23] for an application using this detector). The technique relies on taking experimental observables, in this case the momentum vectors of the 3 α-particle tracks, and applying a constraint/set of constraints. The constraints used here were that the decay conserve both momentum and energy *exactly*. This is important as the measured momentum vectors only conserve momentum and energy approximately as the values are one measurement realization of the true momentum vector's measurand. This technique has been employed in an investigation of the Hoyle decay to 3 α-particles before and showed an enhancement of resolution without biasing the results [23, 24]. It is important to note that ensuring the conservation of energy and momentum does not preferentially bias towards either a sequential or direct decay.

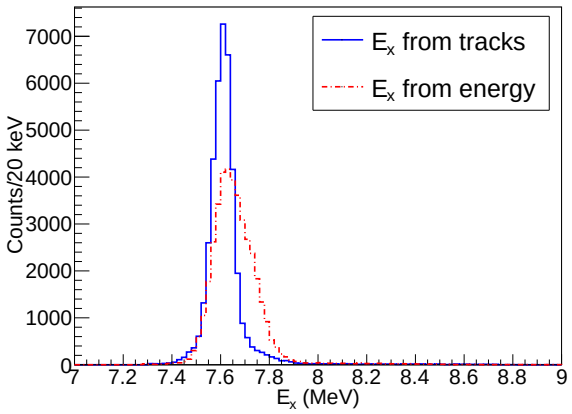

Figure 10: Comparison between calculating the excitation energy using the total energy (calorimetric) versus calculating using the total length of the α-particle tracks. The calorimetric method has a FWHM of 90 keV versus the full track method which has a FWHM of 175 keV.

The 4 constraint equations used for this kinematic fitting were:

$$\sum_{i=1}^{3} \mathbf{p}_{x_i} = 0, \tag{5}$$

$$\sum_{i=1}^{3} \mathbf{p}_{y_i} = 0, \tag{6}$$

$$\sum_{i=1}^{3} \mathbf{p}_{z_i} = 0, \quad \text{and} \tag{7}$$

$$\sum_{i=1}^{3} p_i^2 = 2m_\alpha E_{\text{decay}}. \tag{8}$$

This technique helps identify, and partially correct for, events where a large amount of scattering has occurred and more accurately determine the momentum vector of a short track where the effects of detector pixellation can induce large errors on its direction.

Figure 11a shows a 2D histogram of the angle of each of the two lowest energy α-particles relative to the highest energy α-particle, (see Fig. 12). The large spread in angles can be seen which, by comparing with Fig. 11b, is outside the kinematically allowed region. When enforcing the kinematic fitting technique, almost all the counts can now be seen to be inside of this allowed region and demonstrate a preference for the sequential decay mechanism.

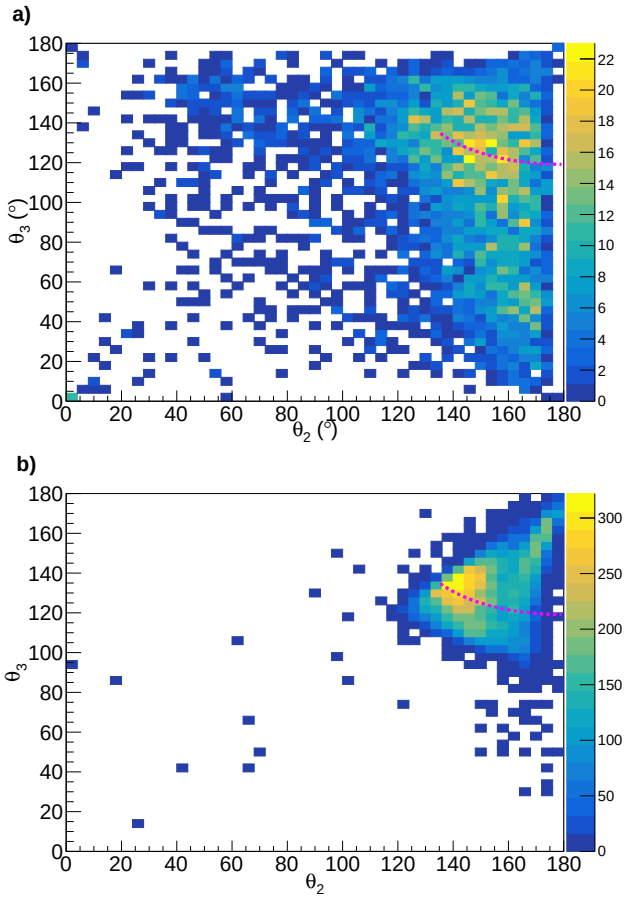

Figure 11: Angle between the longest arm and the other two arms for the decay before (a) and after (b) kinematic fitting. The dotted magenta line overlay shows the locus populated by sequential decays. Direct decays are located around 120° for both θ_2 and θ_3 where the counts can be seen to rapidly decrease.

The spread in this plot is such that some events populate the area where the energy is shared equally between the three α-particles. This area, often called DDE (Direct Decay Equal-energies), represents the most likely configuration for an α-condensate [25]. When incorporating three-body penetrabilities over decays occupying the entire phase space (known as DDΦ), this also manifests itself as looking almost identical to the DDE case (this is known as the DDP^2 model) [26]. In other words, the most preferential three-body decay occurs where all the α-particles have roughly similar energies. Additional constraints to identify this possibility, such as looking at the length of the longest arm, are therefore required to locate the direct decays.

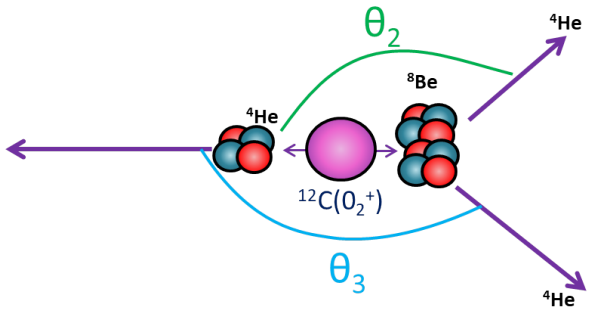

Figure 12: Definition of θ_2 and θ_3 in the lab frame. Both angles are defined relative to the highest energy α-particle (corresponding to that from the first decay in the case of sequential emission).

5. Simulations

5.1. GEANT4 simulations

A GEANT4 [27] simulation package was used to model the response of TexAT to different reactions. This *TexAtSim* program allows for different fill gases and pressures requiring inputs from Magboltz [28] calculations which give the drift velocity as well as the time and position spread of a drift electron. Following the primary event generation, the energy loss of the reaction products throughout the medium is then used to generate electrons along the path consistent with the work function of the gas. These electrons are then drifted towards the Micromegas plate and are smeared in position and time by a Gaussian distribution given by the Magboltz code. The hit positions at the Micromegas are then converted into pseudo-pixels. The outputs of this simulation are the time, position and energy of electrons hitting these pseudopixels.

To model the response of TexAT in terms of the detector segmentation and electronics shaping, a second program, *TexAtResponse*, is used which takes the electron hits for a given Micromegas pad and converts from a charge distribution to a shaped voltage signal in the same way the pre-amp and GET electronics will shape a real signal. This signal is then digitized and the output is a waveform for each Micromegas pad converted to the experimental MFM format. These Monte Carlo simulation data and the real data can then be analyzed in the same way.

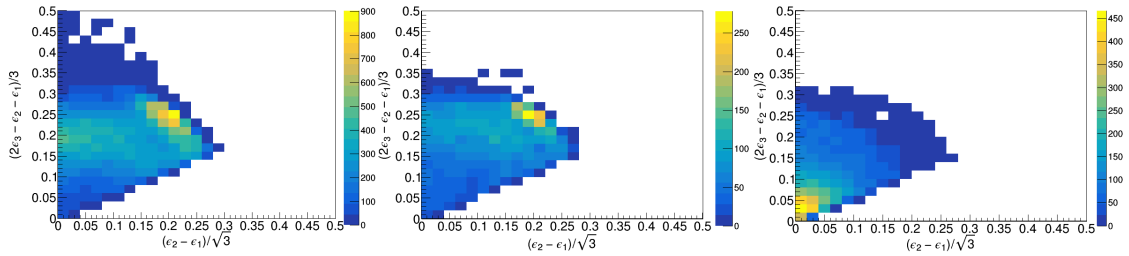

Figure 13: Dalitz plot for the experimental data (left) in comparison to the simulated data for the sequential decay (middle) and direct decays (right).

5.2. 3-α decay

To model the 3-α decay of ^{12}C, a selection between sequential decay through the ^{8}Be(g.s.) and direct decay was possible. The direct decay was chosen with a weighting given by the DDP^2 model which incorporates equal population of the direct decay across the phase space with three-body penetrabilities [26]. This decay mode is also similar to that of the DDE model [25] where the α-particles share their energy smeared only by the Heisenberg uncertainty principle. The results of these simulations indicate that this β-delayed charged-particle decay has a sensitivity comparable to silicon detector arrays. A Dalitz plot showing the data from the current work is shown in Fig. 13 in comparison with the simulated events for direct and sequential decay. While the width of the sequential band is large due to scattering in the TPC gas, the unique nature of the TPCs allow tracking of the particles along their entire length. This means that additional manual (by eye) examination of the events most described as direct is possible and any such scattering along the track of the particles causing a sequential decay to look direct can be excluded. Preliminary measurements show the branching ratio upper limit can be placed below the 1% level proving competitive with the first and second generation of silicon array studies of the Hoyle decay process [6, 24, 29, 30, 31]. The exact details will be outlined in a later paper.

6. Results

6.1. Branching ratios

It is possible in our setup to calculate the branching ratios from ^{12}N β-decay as the total number of L1A triggers (^{12}N events) is recorded and the beam purity is also monitored. For the partial L1A events, the stopping point of the beam can be reconstructed and events selected where the beam stops in the 'safe region' (more than 47 mm from the edge of the Micromegas). By counting the amount of beam ions that stop in this region and comparing this to the number of Hoyle events measured inside this region, one can extract the Hoyle branching ratio directly. This simplicity demonstrates the advantage of 4π coverage detectors operating in single decay mode where no assumptions or other normalization factors need to be included. A well-defined correction must be applied as Hoyle decays are only passed through the analysis code for this purpose between t=1 and 30 ms. This time truncation captures 78.7% of the potential decays.

For higher excitations, the higher energy α-particles always create a successful L1B trigger as these particles have higher energy-deposition tracks than the Hoyle decays. To extract the total 3-α branching ratio, the total number of events in this central region was examined.

Our results presented in Table 1, agree reasonably well with recent measurements [3]. Our results are indicative of a somewhat reduced branching ratio to the bound states and a somewhat larger β-seeding to the Hoyle state and higher-lying states. This suggests a discrepancy in the overall normalization between our result and that used at KVI. Our slightly higher value for the Hoyle branching ratio is also consistent with a higher direct observation of the Hoyle branching ratio using Gammasphere in ^{12}B [1]. The latter saw a 8% higher Hoyle branching ratio than the KVI value which was measured at the same time as the ^{12}N branching ratios although the Gammasphere results have larger statistical uncertainties.

To determine the uncertainties in our measurement, the branching ratio was evaluated for each 1 hour of beam time and the uncertainties were determined from the counting statistics.

The systematic uncertainty was then determined from using the weighted standard deviation between all of these runs. Checks were made to ensure there was no correlation with the pressure or beam rate.

Table 1: Branching ratios for ^{12}C states populated in ^{12}N β^+-decay from the present work and from KVI [3, 32].

State	KVI(%)	Current work(%)
g.s	96.17± 0.05	-
4.44 MeV - 2_1^+	1.90 ± 0.04	-
7.65 MeV - 0_2^+	1.44 ± 0.03	1.58 ± 0.01 (stat.) ± 0.11 (sys.)
7.3-16.3 MeV - 3α	2.11± 0.03	2.54 ± 0.01 (stat.) ± 0.18 (sys.)
$0_2^+/3\alpha$	68 ± 2	62.1 ± 0.4 (stat.) ± 0.2 (sys.)

This current measurement is insensitive to many forms of systematic error. The system is only dead following the initial L1A implantation. Hence, to avoid systematic errors on the number of decays, decay times greater than 1 ms are chosen. Following the measurement of a decay, the beam is sent only after the data acquisition system is no longer busy. The only potential miscounting on the number of particles entering TexAT is for double beam implants. The deadtime for the system following a trigger is 720 μs, which, for an average beam intensity of 60 pps (with no cyclotron phase shifting), means that roughly 4% of beam implantation events will have a second beam arriving during the deadtime of the data acquisition. The exact value was extracted from the IC scalar and was 3.9%. Additionally, one must also account for beam ions that drift in, or out, of the Micromegas region that is selected for Hoyle events before they decay. Given that there is a higher density of beam ions stopping inside the beam region compared to the other side of the position gated region, this will contribute to a systematically smaller branching ratio determination than the true value. Given the random displacement distance is small compared to the stopping position in the gas, it is therefore assumed that the number of ions that stop outside the gated region and enter in for the decay is equal to those that stop inside the gated region and exit for the decay and therefore the systematic error from this effect is small.

6.2. Half-life measurement

The time between the L1A and L1B trigger is digitized following the writing of the event. One can therefore extract a clean half-life measurement from our data by ensuring the L1B trigger corresponds to a good decay of ^{12}N. It is important to note however that the 'stop' and 'start' of these triggers do not correspond exactly to the event of interest as shown in Fig. 14. The 'start/stop' signal actually arrives following the arrival of the first drifted electrons onto the Micromegas detector. To ensure that a clean selection is made on the L1A/L1B event, only events corresponding to the Hoyle state are selected. This removes any contribution from background events seen in the gas. These typically occur by tracks entering from outside on the Micromegas region and are vetoed by the previous selection. Additionally, the decays within the first 1 ms are omitted as this is where possible beam + beam events can occur which should also be excluded by the event selection. The results after these cuts have been applied are shown in Fig. 15. One must also estimate the contribution to this half-life measurement from instances where one ^{12}N ion is implanted within TexAT, no decay is observed within 30 ms so the phase shifter is turned back on and then another ^{12}N is implanted after t_d and then the decay from the *first* ^{12}N occurs. The differential probability of the decay is given by $\exp(-t_d/t_0)$ where $t_0 = \frac{t_{1/2}}{\ln(2)}$. With an average of $\sim$ 35 ms between implantation events (with $\sim$ 30 pps), this probability is 4%. Therefore, this probability is suppressed by this factor where t_d here corresponds to the time between the two implantations. The probability of this misidentification is further reduced by selecting events where the decay and beam stop are correlated. This reduces the random coincidences, ϵ by a factor of 10 to 0.4%. The fitted function therefore has the form:

$$A(1-\epsilon)\exp(-t/t_0) + \epsilon A \exp(-2t/t_0), \tag{9}$$

with t_0 as the decay constant and ϵ being the random coincidence value. A binned-likelihood method was used to overcome any issues caused by small n deviations from the central limit theorem. Half of the magnitude of this multiple implant correction is given as a systematic error (0.01 ms). The obtained $t_{1/2}$ value is 10.92 $\pm$ 0.11 (stat.) $\pm$ 0.01 (sys.) ms, a value consistent with the previously measured value of 11.000 $\pm$ 0.016 ms. This result is

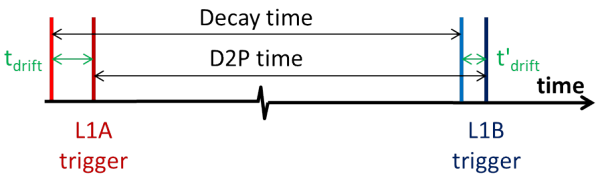

Figure 14: The D2P time measures the time between the L1A and L1B trigger but this does not give the decay time. One must also ensure that the drift time for the L1A and L1B triggers are taken into account to convert to the time between decays.

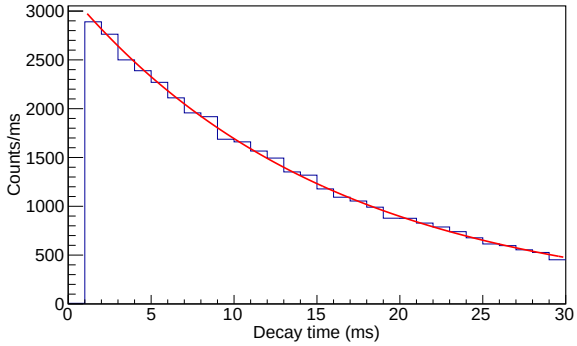

Figure 15: Decay time spectrum for ^{12}N $\rightarrow$ ^{12}C(0_2^+). The fitted value for $t_{1/2}$ is 10.92 $\pm$ 0.11 (stat.) $\pm$ 0.01 (sys.) ms.

obtained without any need for inclusion of a background demonstrating not only the high background rejection level but the use of the D2P time between L1A and L1B triggers accurately represents the known half-life for ^{12}N at the 1% accuracy level.

7. Conclusion

The TexAT device in conjunction with GET is able to measure the β-delayed particle decay and measure the phase space of subsequent three-body reactions. The time separation between the implant and decay can extend up to 1.677 s with GET and using the decay-by-decay method in conjunction with correlating the beam stopping position with the decay vertex, a very low background can be achieved. The results for the branching ratio of ^{12}N to states in ^{12}C above the 3-α threshold agree with previous measurements and the total branching ratio to the Hoyle state is 1.58% $\pm$ 0.01% (stat.) $\pm$ 0.11% (sys.). This value

is in agreement with recent studies [3] of both ^{12}B and ^{12}N using α-spectroscopy at KVI and Jyväskylä. Our backgroundless measurement of the ^{12}N half-life, using the β-delayed charged-particle-decay, is $t_{1/2} = 10.92 \pm 0.11$ (stat.) $\pm$ 0.01 (sys.) ms. This value agrees with the accepted value.

8. Acknowledgments

TexAT project was supported by the U.S. Department of Energy, Office of Science, Office of Nuclear Science, under Award No. DE-FG02-93ER40773 and by National Nuclear Security Administration through the Center for Excellence in Nuclear Training and University Based Research (CENTAUR) under grant number #de-na0003841. G.V.R. also acknowledges the support of the Nuclear Solutions Institute.

References

[1] M. Munch, M. Alcorta, H. O. U. Fynbo, M. Albers, S. Almaraz-Calderon, M. L. Avila, A. D. Ayangeakaa, B. B. Back, P. F. Bertone, P. F. F. Carnelli, M. P. Carpenter, C. J. Chiara, J. A. Clark, B. DiGiovine, J. P. Greene, J. L. Harker, C. R. Hoffman, N. J. Hubbard, C. L. Jiang, O. S. Kirsebom, T. Lauritsen, K. L. Laursen, S. T. Marley, C. Nair, O. Nusair, D. Santiago-Gonzalez, J. Sethi, D. Seweryniak, R. Talwar, C. Ugalde, S. Zhu, Independent measurement of the hoyle state β feeding from ^{12}B using gammasphere, Phys. Rev. C 93 (2016) 065803 (Jun 2016). doi:10.1103/PhysRevC.93.065803.

[2] Y. Kanada-En'yo, The structure of ground and excited states of12c, Progress of Theoretical Physics 117 (4) (2007) 655–680, cited By 156 (2007). doi:10.1143/PTP.117.655.

[3] S. Hyldegaard, C. Forssén, C. Diget, M. Alcorta, F. Barker, B. Bastin, M. Borge, R. Boutami, S. Brandenburg, J. Büscher, P. Dendooven, P. V. Duppen, T. Eronen, S. Fox, B. Fulton, H. Fynbo, J. Huikari, M. Huyse, H. Jeppesen, A. Jokinen, B. Jonson, K. Jungmann, A. Kankainen, O. Kirsebom, M. Madurga, I. Moore, P. Navrátil, T. Nilsson, G. Nyman, G. Onderwater, H. Penttilä, K. Peräjärvi, R. Raabe, K. Riisager, S. Rinta-Antila, A. Rogachevskiy, A. Saastamoinen, M. Sohani, O. Tengblad, E. Traykov, J. Vary, Y. Wang, K. Wilhelmsen, H. Wilschut, J. Äystö, Precise branching ratios to unbound 12c states from 12n and 12b β-decays, Physics Letters B 678 (5) (2009) 459 – 464 (2009). doi:https://doi.org/10.1016/j.physletb.2009.06.064.

[4] E. Pollacco, L. Trache, E. Simmons, A. Spiridon, M. McCleskey, B. Roeder, A. Saastamoinen, R. Tribble, G. Pascovici, M. Kebbiri, J. Mols, M. Raillot, Astrobox: A novel detection system for very low-energy protons from beta-delayed proton decay, Nuclear Instruments and Methods in Physics Research

Section A: Accelerators, Spectrometers, Detectors and Associated Equipment 723 (2013) 102 – 108 (2013). doi:https://doi.org/10.1016/j.nima.2013.04.084.

[5] M. Freer, H. Fynbo, The hoyle state in 12c, Progress in Particle and Nuclear Physics 78 (2014) 1 – 23 (2014). doi:https://doi.org/10.1016/j.ppnp.2014.06.001.

[6] J. Manfredi, R. J. Charity, K. Mercurio, R. Shane, L. G. Sobotka, A. H. Wuosmaa, A. Banu, L. Trache, R. E. Tribble, α decay of the excited states in ^{12}c at 7.65 and 9.64 mev, Phys. Rev. C 85 (2012) 037603 (Mar 2012). doi:10.1103/PhysRevC.85.037603.

[7] R. Smith, Tz. Kokalova, C. Wheldon, J. E. Bishop, M. Freer, N. Curtis, D. J. Parker, New measurement of the direct 3α decay from the ^{12}C hoyle state, Phys. Rev. Lett. 119 (2017) 132502 (Sep 2017). doi:10.1103/PhysRevLett.119.132502.

[8] D. Dell'Aquila, I. Lombardo, G. Verde, M. Vigilante, L. Acosta, C. Agodi, F. Cappuzzello, D. Carbone, M. Cavallaro, S. Cherubini, A. Cvetinovic, G. D'Agata, L. Francalanza, G. L. Guardo, M. Gulino, I. Indelicato, M. La Cognata, L. Lamia, A. Ordine, R. G. Pizzone, S. M. R. Puglia, G. G. Rapisarda, S. Romano, G. Santagati, R. Spartà, G. Spadaccini, C. Spitaleri, A. Tumino, High-precision probe of the fully sequential decay width of the hoyle state in ^{12}C, Phys. Rev. Lett. 119 (2017) 132501 (Sep 2017). doi:10.1103/PhysRevLett.119.132501.

[9] T. Rana, S. Bhattacharya, C. Bhattacharya, S. Manna, S. Kundu, K. Banerjee, R. Pandey, P. Roy, A. Dhal, G. Mukherjee, V. Srivastava, A. Dey, A. Chaudhuri, T. Ghosh, A. Sen, M. Asgar, T. Roy, J. Sahoo, J. Meena, A. Saha, R. Saha, M. Sinha, A. Roy, New high precision study on the decay width of the hoyle state in 12c, Physics Letters B 793 (2019) 130 – 133 (2019). doi:https://doi.org/10.1016/j.physletb.2019.04.028.

[10] E. Koshchiy, G. Rogachev, E. Pollacco, S. Ahn, E. Uberseder, J. Hooker, J. Bishop, E. Aboud, M. Barbui, V. Goldberg, C. Hunt, H. Jayatissa, C. Magana, R. O'Dwyer, B. Roeder, A. Saastamoinen, S. Upadhyayula, Texas active target (texat) detector for experiments with rare isotope beams, Nuclear Instruments and Methods in Physics Research Section A: Accelerators, Spectrometers, Detectors and Associated Equipment 957 (2020) 163398 (2020). doi:https://doi.org/10.1016/j.nima.2020.163398. URL `http://www.sciencedirect.com/science/article/pii/S0168900220300073`

[11] J. Hooker, G. V. Rogachev, E. Koshchiy, S. Ahn, M. Barbui, V. Z. Goldberg, C. Hunt, H. Jayatissa, E. C. Pollacco, B. T. Roeder, A. Saastamoinen, S. Upadhyayula, Structure of ^{9}C through proton resonance scattering with the texas active target detector, Phys. Rev. C 100 (2019) 054618 (Nov 2019). doi:10.1103/PhysRevC.100.054618.

[12] P. Fonte, V. Peskov, F. Sauli, Feedback and breakdown in parallel-plate chambers, Nuclear Instruments and Methods in Physics Research Section A: Accelerators, Spectrometers, Detectors and Associated Equipment 305 (1) (1991) 91 – 110 (1991). doi:https://doi.org/10.1016/0168-9002(91)90522-R.

497 URL http://www.sciencedirect.com/science/article/pii/016890029190522R
498 [13] F. Sauli, The gas electron multiplier (gem): Operating principles and applications, Nuclear In-
499 struments and Methods in Physics Research Section A: Accelerators, Spectrometers, Detectors and
500 Associated Equipment 805 (2016) 2 – 24, special Issue in memory of Glenn F. Knoll (2016).
501 doi:https://doi.org/10.1016/j.nima.2015.07.060.
502 [14] R. Tribble, R. Burch, C. Gagliardi, Mars: A momentum achromat recoil spectrometer, Nuclear Instru-
503 ments and Methods in Physics Research Section A: Accelerators, Spectrometers, Detectors and Asso-
504 ciated Equipment 285 (3) (1989) 441 – 446 (1989). doi:https://doi.org/10.1016/0168-9002(89)90215-5.
505 [15] F. Paschen, Ueber die zum funkenübergang in luft, wasserstoff und kohlensäure bei verschiede-
506 nen drucken erforderliche potentialdifferenz, Annalen der Physik 273 (5) (1889) 69–96 (1889).
507 doi:10.1002/andp.18892730505.
508 [16] E. Pollacco, G. Grinyer, F. Abu-Nimeh, T. Ahn, S. Anvar, A. Arokiaraj, Y. Ayyad, H. Baba, M. Babo,
509 P. Baron, D. Bazin, S. Beceiro-Novo, C. Belkhiria, M. Blaizot, B. Blank, J. Bradt, G. Cardella, L. Car-
510 penter, S. Ceruti, E. D. Filippo, E. Delagnes, S. D. Luca, H. D. Witte, F. Druillole, B. Duclos, F. Favela,
511 A. Fritsch, J. Giovinazzo, C. Gueye, T. Isobe, P. Hellmuth, C. Huss, B. Lachacinski, A. Laffoley,
512 G. Lebertre, L. Legeard, W. Lynch, T. Marchi, L. Martina, C. Maugeais, W. Mittig, L. Nalpas,
513 E. Pagano, J. Pancin, O. Poleshchuk, J. Pedroza, J. Pibernat, S. Primault, R. Raabe, B. Raine,
514 A. Rebii, M. Renaud, T. Roger, P. Roussel-Chomaz, P. Russotto, G. Saccà, F. Saillant, P. Sizun,
515 D. Suzuki, J. Swartz, A. Tizon, N. Usher, G. Wittwer, J. Yang, Get: A generic electronics system for
516 tpcs and nuclear physics instrumentation, Nuclear Instruments and Methods in Physics Research Sec-
517 tion A: Accelerators, Spectrometers, Detectors and Associated Equipment 887 (2018) 81 – 93 (2018).
518 doi:https://doi.org/10.1016/j.nima.2018.01.020.
519 [17] J. Kelley, J. Purcell, C. Sheu, Energy levels of light nuclei a=12, Nuclear Physics A 968 (2017) 71 –
520 253 (2017). doi:https://doi.org/10.1016/j.nuclphysa.2017.07.015.
521 [18] S. Anvar, R. Fox, B. Raine, F. Saillant, N. Usher, MFM the multiframe metaformat specification (2.2).
522 URL https://informatique.in2p3.fr/?q=system/files/MultiFrame-2.2.pdf
523 [19] R. O. Duda, P. E. Hart, Use of the hough transformation to detect lines and curves in pictures, Commun.
524 ACM 15 (1) (1972) 11–15 (Jan. 1972). doi:10.1145/361237.361242.
525 [20] M. Morháč, J. Kliman, V. Matoušek, M. Veselský, I. Turzo, Efficient one- and two-dimensional gold
526 deconvolution and its application to gamma-ray spectra decomposition, Nuclear Instruments and Meth-
527 ods in Physics Research Section A: Accelerators, Spectrometers, Detectors and Associated Equipment
528 401 (2) (1997) 385 – 408 (1997). doi:https://doi.org/10.1016/S0168-9002(97)01058-9.
529 URL http://www.sciencedirect.com/science/article/pii/S0168900297010589
530 [21] E. H. Beckner, C. M. Jones, G. C. Phillips, Evidence for sequential two-body decay in three-body decay

of ^{12}c and ^{10}b, Phys. Rev. 123 (1961) 255–261 (Jul 1961). doi:10.1103/PhysRev.123.255.

[22] G. Forden, D. Saxon, Improving vertex position determination by using a kinematic fit, Nuclear Instruments and Methods in Physics Research Section A: Accelerators, Spectrometers, Detectors and Associated Equipment 248 (2) (1986) 439 – 450 (1986). doi:https://doi.org/10.1016/0168-9002(86)91031-4.

[23] R. Smith, J. Bishop, A fast universal kinematic fitting code for low-energy nuclear physics: Funki_fit, Physics 1 (3) (2019) 375–391 (2019). doi:10.3390/physics1030027.

[24] O. S. Kirsebom, M. Alcorta, M. J. G. Borge, M. Cubero, C. A. Diget, L. M. Fraile, B. R. Fulton, H. O. U. Fynbo, D. Galaviz, B. Jonson, M. Madurga, T. Nilsson, G. Nyman, K. Riisager, O. Tengblad, M. Turrión, Improved limit on direct α decay of the hoyle state, Phys. Rev. Lett. 108 (2012) 202501 (May 2012). doi:10.1103/PhysRevLett.108.202501.

[25] J. Bishop, R. Smith, T. Kokalova, C. Wheldon, N. Curtis, M. Freer, D. Parker, An improved upper limit on the direct 3-α decay of the hoyle state, AIP Conference Proceedings 2038 (1) (2018) 020035 (2018). doi:10.1063/1.5078854.

[26] R. Smith, Experimental measurements of break-up reactions to study alpha clustering in carbon-12 and beryllium-9, Ph.D. thesis, University of Birmingham (2017).

[27] S. Agostinelli, J. Allison, K. Amako, J. Apostolakis, H. Araujo, P. Arce, M. Asai, D. Axen, S. Banerjee, G. Barrand, F. Behner, L. Bellagamba, J. Boudreau, L. Broglia, A. Brunengo, H. Burkhardt, S. Chauvie, J. Chuma, R. Chytracek, G. Cooperman, G. Cosmo, P. Degtyarenko, A. Dell'Acqua, G. Depaola, D. Dietrich, R. Enami, A. Feliciello, C. Ferguson, H. Fesefeldt, G. Folger, F. Foppiano, A. Forti, S. Garelli, S. Giani, R. Giannitrapani, D. Gibin, J. G. Cadenas, I. González, G. G. Abril, G. Greeniaus, W. Greiner, V. Grichine, A. Grossheim, S. Guatelli, P. Gumplinger, R. Hamatsu, K. Hashimoto, H. Hasui, A. Heikkinen, A. Howard, V. Ivanchenko, A. Johnson, F. Jones, J. Kallenbach, N. Kanaya, M. Kawabata, Y. Kawabata, M. Kawaguti, S. Kelner, P. Kent, A. Kimura, T. Kodama, R. Kokoulin, M. Kossov, H. Kurashige, E. Lamanna, T. Lampén, V. Lara, V. Lefebure, F. Lei, M. Liendl, W. Lockman, F. Longo, S. Magni, M. Maire, E. Medernach, K. Minamimoto, P. M. de Freitas, Y. Morita, K. Murakami, M. Nagamatu, R. Nartallo, P. Nieminen, T. Nishimura, K. Ohtsubo, M. Okamura, S. O'Neale, Y. Oohata, K. Paech, J. Perl, A. Pfeiffer, M. Pia, F. Ranjard, A. Rybin, S. Sadilov, E. D. Salvo, G. Santin, T. Sasaki, N. Savvas, Y. Sawada, S. Scherer, S. Sei, V. Sirotenko, D. Smith, N. Starkov, H. Stoecker, J. Sulkimo, M. Takahata, S. Tanaka, E. Tcherniaev, E. S. Tehrani, M. Tropeano, P. Truscott, H. Uno, L. Urban, P. Urban, M. Verderi, A. Walkden, W. Wander, H. Weber, J. Wellisch, T. Wenaus, D. Williams, D. Wright, T. Yamada, H. Yoshida, D. Zschiesche, Geant4—a simulation toolkit, Nuclear Instruments and Methods in Physics Research Section A: Accelerators, Spectrometers, Detectors and Associated Equipment 506 (3) (2003) 250 – 303 (2003). doi:https://doi.org/10.1016/S0168-9002(03)01368-8.

[28] S. F. Biagi, Magboltz 8.
URL http://magboltz.web.cern.ch/magboltz

[29] M. Freer, A. H. Wuosmaa, R. R. Betts, D. J. Henderson, P. Wilt, R. W. Zurmühle, D. P. Balamuth, S. Barrow, D. Benton, Q. Li, Z. Liu, Y. Miao, Limits for the 3α branching ratio of the decay of the 7.65 mev, 0_2^+ state in ^{12}C, Phys. Rev. C 49 (1994) R1751–R1754 (Apr 1994). doi:10.1103/PhysRevC.49.R1751.
URL https://link.aps.org/doi/10.1103/PhysRevC.49.R1751

[30] A. Raduta, B. Borderie, E. Geraci, N. L. Neindre, P. Napolitani, M. Rivet, R. Alba, F. Amorini, G. Cardella, M. Chatterjee, E. D. Filippo, D. Guinet, P. Lautesse, E. L. Guidara, G. Lanzalone, G. Lanzano, I. Lombardo, O. Lopez, C. Maiolino, A. Pagano, S. Pirrone, G. Politi, F. Porto, F. Rizzo, P. Russotto, J. Wieleczko, Evidence for alpha-particle condensation in nuclei from the hoyle state deexcitation, Physics Letters B 705 (1) (2011) 65 – 70 (2011). doi:https://doi.org/10.1016/j.physletb.2011.10.008.
URL http://www.sciencedirect.com/science/article/pii/S0370269311012408

[31] T. K. Rana, S. Bhattacharya, C. Bhattacharya, S. Kundu, K. Banerjee, T. K. Ghosh, G. Mukherjee, R. Pandey, P. Roy, V. Srivastava, M. Gohil, J. K. Meena, H. Pai, A. K. Saha, J. K. Sahoo, R. M. Saha, Estimation of direct components of the decay of the hoyle state, Phys. Rev. C 88 (2013) 021601 (Aug 2013). doi:10.1103/PhysRevC.88.021601.
URL https://link.aps.org/doi/10.1103/PhysRevC.88.021601

[32] S. Hyldegaard, Beta-decay studies of 8be and 12c, Ph.D. thesis, Aarhus University (2010).